

Inertial blob-hole symmetry breaking in magnetised plasma filaments

Alexander Kendl

*Institute for Ion Physics and Applied Physics,
University of Innsbruck, Association Euratom-ÖAW,
Technikerstr. 25, 6020 Innsbruck, Austria*

Abstract

Symmetry breaking between the propagation velocities of magnetised plasma filaments with large positive (blob) and negative (hole) amplitudes, as implied by a dimensional analysis scaling, is studied with global (“full-n”) non-Boussinesq gyrofluid computations, which include finite inertia effects through nonlinear polarisation. Interchange blobs on a flat density background have higher inertia and propagate more slowly than holes. In the presence of a large enough density gradient, the effect is reversed: blobs accelerate down the gradient and holes are slowed in their propagation up the gradient. Drift wave blobs spread their initial vorticity rapidly into a fully developed turbulent state, whereas primary holes can remain coherent for many eddy turnover times. The results bear implications for plasma edge zonal flow evolution and tokamak scrape-off-layer transport.

This is a preprint version of a manuscript submitted to “Plasma Physics and Controlled Fusion”.

I. INTRODUCTION

Localised pressure perturbations in magnetised plasmas are commonly referred to as blobs for positive amplitudes $+\delta p$ in relation to the background pressure p , and as holes for negative amplitudes $-\delta p$. Pressure perturbations extend along the magnetic field lines into filaments, whereas the motion perpendicular to the magnetic field \mathbf{B} is principally determined by drifts. In presence of a magnetic field inhomogeneity the curvature and gradient-B drifts induce a dipolar potential structure, and the resulting electric field's $E \times B$ drift drives the perturbations. Blobs travel down (and vice versa holes up) a mean gradient [1].

This propagation of blob filaments constitutes the major cross-field transport mechanism for plasma density and heat in the scrape-off layer (SOL) of tokamak fusion experiments, and is observed in many other magnetised laboratory or natural plasmas [2–4]. SOL interchange turbulence is considered to be composed of an ensemble of nonlinearly interacting blobs and holes [5]. Both blobs and holes appear to be primarily generated in the vicinity of the separatrix, and can be experimentally identified by the sign of the skewness in the probability distribution function of fluctuation amplitudes [6, 7]. The underlying interchange instability and the shape evolution of a plasma blob into plumes share many features with the buoyancy driven Rayleigh-Taylor instability in neutral fluids [9].

A common assumption presumes the propagation of blobs and holes to be symmetric under simultaneous reversal of (C) the sign of the amplitude (blobs or holes respectively) and of (P) the direction specified by the gradient of the magnetic field. This combined CP symmetry is indeed well fulfilled for blobs and holes with small amplitudes $\pm\delta p \ll p$ relative to the background plasma. Turbulence driven pressure fluctuations in the edge and SOL of magnetised fusion plasmas however can have amplitudes in the order of unity [7, 8, 10–12], and even above, as the propagation of edge-localised mode (ELM) filaments in the SOL is similar to large blobs [13].

The propagation and fragmentation of pressure perturbations like blobs is for large amplitudes influenced by inertial (“global”) effects mediated mainly through nonlinear polarisation [14]. Most models and numerical codes for plasma blob propagation and edge turbulence so far have however been making use of the delta-n or Boussinesq approximation, which assumes small fluctuation amplitudes. The inertial and nonlinear polarisation effects on drift wave turbulence and blob propagation significantly modify the picture of edge and

SOL fluctuations. Recent results for global blob propagation obtained with non-Boussinesq codes and models [14–18] demonstrate the relevance of full-n modelling in the edge for more realistic SOL blob transport scalings: large inertial blobs are slowed on flat background profiles, but accelerate strongly down pressure gradients.

In light of these results on large inertial blobs it appears not at all any more evident that large amplitude blobs and holes should be CP symmetric. The following work numerically studies asymmetries between inertial interchange blobs and holes (2-d), and between large amplitude drift vortices (3-d) with initially different polarities. The computational implementation is based on an isothermal reduction of the full-n gyrofluid model by Madsen [19], and reduces to the delta-n model (GEM3) by Scott [20, 27] in the limit of small fluctuation amplitudes, and to the full-n model by Wiesenberger [14] in the two-dimensional limit.

II. MODEL AND NUMERICAL METHODS

The full-n 3-d gyrofluid model by Madsen [19] consists of a set of 6-moment equations and of the field equations for the potentials, completed by a first order finite Larmor radius closure. In the following, an isothermal plasma is assumed, where temperature variations in space and time are neglected. A normalised energetically consistent set of 3-d full-n isothermal gyrofluid equations for electrons and ions (species $s \in e, i$) for the first two moments (corresponding to eqs. 22 and 23 in ref. [19]), which are the gyrocenter densities n_s and parallel velocities v_s , is:

$$\partial_t \hat{n}_s = \frac{1}{B} [\hat{n}_s, \phi_s] - \frac{B}{n_s} \nabla_{\parallel} \left(\frac{n_s v_s}{B} \right) + \kappa(h_s) \quad (1)$$

$$\partial_t \alpha_s = \frac{\mu_s}{B} [v_s, \phi_s] - \nabla_{\parallel} h_s - C \frac{J_{\parallel}}{n_s} + \mu_s \tau_s v_s \kappa(\hat{n}_s) + 2\mu_s \tau_s \kappa(v_s) \quad (2)$$

with $\alpha_s \equiv (\beta_0 A_{\parallel} + \mu_s v_s)$ and $h_s \equiv (\phi_s + \tau_s \hat{n}_s)$. Triple nonlinear terms including the parallel velocity are here neglected. The nonlinear polarisation equation

$$\sum_s \left[Z_s e \Gamma_{1s} n_s + \nabla \cdot \left(n_s \frac{|\mu_s|}{B^2} \nabla \right) \phi \right] = 0. \quad (3)$$

determines the electrostatic potential ϕ . The gyro-screened potential is given by $\phi_s = \Gamma_{1s} \phi - (\mu_s/2B)(\nabla \phi)^2$. Parallel velocities and current are coupled to the vector potential A_{\parallel} via Ampere's law $\nabla_{\perp}^2 A_{\parallel} = -J_{\parallel} = -\sum_s n_s Z_s e v_s$. The gyro-averaging operator in Padé

approximation is defined by $\Gamma_{1s} = (1 + (1/2)b_s)^{-1}$ with $b_s = \tau_s \mu_s \nabla_\perp^2$. The mass ratio is given by $\mu_s = m_s / (Z_s m_i)$, and the (constant) temperature ratio by $\tau_s = T_s / (Z_s T_e)$. For electrons, thus $\tau_e = -1$, and finite Larmor radius (FLR) effects are neglected ($b_e \equiv 0$). The electron contribution to the polarisation in eq. (3) is also neglected, as $|\mu_e| \ll |\mu_i|$. The gyrocenter densities n_s are normalised to a constant reference density n_0 , so that the magnitude of the plasma density $n_s \leftarrow n_s/n_0$ is of order one. Eqs. (1, 2) have been divided by the specific variable densities n_s , and logarithmic densities $\hat{n}_s \equiv \ln n_s$ are introduced to ensure positivity, with both \hat{n}_s and n_s appearing in the equations.

The spatial derivative operators are normalised as $\nabla \leftarrow \rho_s \nabla$ to the drift scale $\rho_s = (c/eB_0)\sqrt{m_i T_e}$, where m_i is the mass of the main ion species, T_e is a constant reference electron temperature, and B_0 is a static reference background magnetic field strength. Parallel derivatives are further scaled as $\nabla_\parallel \leftarrow (L_\parallel/L_\perp)\nabla_\parallel$ with the connection length L_\parallel , which for toroidal geometry is given by $L_\parallel = 2\pi qR$ with inverse rotational transform q and major torus radius R . The drift parameter $\delta = \rho_s/L_\perp$ is used to set the perpendicular length scale L_\perp . For blob simulations often $L_\perp = \rho_s$ is used (so that $\delta = 1$), and for gradient driven turbulence usually $L_\perp = L_n$ is set as the density gradient length scale L_n . In order to apply the same normalisation length for all presented simulations (including those on drift wave vortices), a normalisation to a typical edge gradient length is chosen with $\delta = 0.01$.

The time scale is normalised as $\partial_t \leftarrow (\rho_s/c_s)\partial_t$, and parallel velocities $v_{\parallel s} \leftarrow v_{\parallel s}/c_s$ are normalised by the sound speed $c_s = \sqrt{T_e/m_i}$. Further, $\phi \leftarrow (e\phi/T_e)$, $B \leftarrow B/B_0$, $J_\parallel \leftarrow J_\parallel/(en_0 c_s)$, and $A_\parallel \leftarrow (A_\parallel/\beta_0 B_0 \rho_0)(L_\perp/qR)$ for a reference electron beta given by $\beta_0 = 4\pi n_0 T_{e0}/B_0^2$. The collisionality parameter is given by $C = (L_\perp/c_s \rho_0 B_0)\eta$ with $\eta = 0.51(m_e \nu_e)/(n_0 e^2)$. The main plasma parameters are $\hat{\mu}_s = \mu_s \hat{\epsilon}$, $\hat{\beta} = (n_0 T_e/B_0^2)\hat{\epsilon}$, and $\hat{C} = 0.51(m_e \nu_e L_\perp/c_{s0})\hat{\epsilon}$ with $\hat{\epsilon} = (qR/L_\perp)^2$. In the following only electrostatic blobs and vortices with $\hat{\beta} = 0$ are discussed (while electromagnetic effects are of more relevance for fully developed turbulence).

The 2-d advection terms are expressed through Poisson brackets $[f, g] = (\partial_x f)(\partial_y g) - (\partial_y f)(\partial_x g)$ for locally perpendicular coordinates x and y . Normal and geodesic components of the magnetic curvature enter the compressional effect due to field inhomogeneity by $\hat{\kappa} = \hat{\kappa}_y \partial_y + \hat{\kappa}_x \partial_x$ where the curvature components in toroidal geometry are functions of the poloidal angle θ mapped onto the parallel coordinate z . For a circular torus $\hat{\kappa}_y \equiv$

$\kappa_0 \cos(z)$ and $\hat{\kappa}_x \equiv \kappa_0 \sin(z)$ when $z = 0$ is defined at the outboard midplane. An Arakawa-Karniadakis numerical scheme [21–23] is used for the computation of eqs. (1) and (2). The generalised Poisson type equation (3) is solved by a Chebyshev accelerated 4th order red-black SOR scheme [24–26]. For numerical stability, a small perpendicular hyper-viscosity term $s_\nu = -\nu_4 \nabla_\perp^4 \hat{n}_s$ is added on the right hand side of eq. (1), and in 3-d computations parallel viscous terms $\nu_\parallel \partial_z^2 \hat{n}_s$ and $\nu_\parallel \partial_z^2 v_s$ are added to eqs. (1) and (2), respectively.

Boundary conditions in y direction are periodic for 2-d simulations, and quasi-periodic (shear-shifted flux tube) for 3-d simulations. The total density is allowed to evolve freely, although for the present short blob propagation times the initial background profiles do not evolve visibly. To avoid degradation and flows at the radial boundaries, fixed mixed (von Neumann / Dirichlet) vorticity free ($n_e = \Gamma_1 n_i$) boundary conditions are applied in x . For longer turbulence simulations with free profile evolution, sources and sinks would rather have to be specified at the radial boundaries.

The delta- n isothermal electromagnetic gyrofluid model [27, 28] is regained by splitting $n_s = n_{s0} + \tilde{n}_s$ into a static constant background density n_{s0} and the perturbed density \tilde{n}_s . When $\tilde{n}_s/n_{s0} \ll 1$, the right hand sides of eqs. (1) and (2) can be linearised by approximating $n_s \approx n_{s0}$ so that $\hat{n}_s \approx \hat{n}_{s0} + (\tilde{n}_s/n_{s0})$, and neglecting all nonlinear terms except the Poisson bracket:

$$\partial_t \tilde{n}_s = \frac{1}{B} [\tilde{n}_s, \tilde{\phi}] - B \nabla_\parallel (\tilde{v}_s/B) + \hat{\kappa}(h_s) \quad (4)$$

$$\partial_t \alpha_s = \frac{\mu_s}{B} [\tilde{v}_s, \tilde{\phi}] - \nabla_\parallel h_s + 2\mu_s \tau_s \hat{\kappa}(\tilde{v}_s) - C J_\parallel \quad (5)$$

The consistent delta- n polarisation equation in the high- k limit is

$$\sum_s a_s [\Gamma_{1s} \tilde{n}_s + (1/\tau_s)(\Gamma_{0s} - 1)\tilde{\phi}] = 0 \quad (6)$$

with $\Gamma_{0s} = (1 + b_s)^{-1}$. Linearisation of the low- k eq. (3) actually does not include the gyro-screening on the potential and results in $\sum_s a_s \Gamma_{1s} \tilde{n}_s = \nabla_\perp^2 \tilde{\phi}$. The velocities and current are again coupled to the parallel component of the fluctuating vector potential by Ampere's equation $\nabla_\perp^2 \tilde{A}_\parallel = \tilde{J}_\parallel = \sum_s a_s \tilde{v}_s$. The parameter $a_s = Z_s n_{s0}/n_{e0}$ describes the ratio of species reference densities n_{s0} to n_{e0} .

III. LARGE INERTIAL 2-D INTERCHANGE BLOBS AND HOLES

In the following, large amplitude blob and hole propagation is compared for the full-n and delta-n models. To separate 2-d interchange and 3-d drift wave effects, at first the computations are restricted to 2-d by neglecting the parallel velocity and parallel derivatives. In this limit the equations correspond to the 2-d full-n model by Wiesenberger [14].

Blobs and holes are initialised as Gaussian density perturbations with width $r = 10\rho_s$ and amplitude $\Delta n = \pm 0.75$ for $n_b = 1$. In the full-n model n_b corresponds to the actual background plasma density, whereas in the delta-n model this can be regarded as a dummy parameter on which the solution does not depend, as the model already implies a large underlying background $n_0 \gg \Delta n$. Dimensional analysis roughly estimates the delta-n and full-n blob propagation speed scalings [14, 17] as

$$\frac{V_{\text{delta}}}{c_s} \sim \sqrt{\Delta n}, \quad \text{and} \quad (7)$$

$$\frac{V_{\text{full}}}{c_s} \sim \sqrt{\frac{\Delta n}{(n_b + \Delta n)}}. \quad (8)$$

On this basis inertial blobs could be expected to propagate more slowly than holes (with reverse direction) in the full-n model.

Simulation parameters here are $\kappa = 0.05$, $\delta = 0.01$ and $\tau_i = 0$. The computational grid is $n_x \times n_y = 512 \times 256$ with resolution $(192 \times 96)\rho_s$. Fig. 1 (top) shows the symmetric evolution of blobs and holes in the delta-n model (top) for times $t = 0$, $t = 12.5$ and $t = 25$. For simultaneous reversal of grad-B direction and sign of the amplitude, delta-n blob and hole coincide: the density contours are identical for blobs and (reversed) holes. The bottom figures show the different states at $t = 25$ for an inertial full-n blob (left) and full-n hole (right). The inertial blob has a more coherent head and, propagates slower than for the delta-n case, whereas the inertial hole fragments more strongly and propagates faster, as predicted by the inertial scaling.

Fig. 2 (left) shows the corresponding time evolution of the x-coordinates of the center of mass (bottom lines) and the propagation fronts (upper lines) for the delta-n case (black dashed lines), the inertial blob (thin red lines) and inertial hole (bold blue lines, mirrored in x direction).

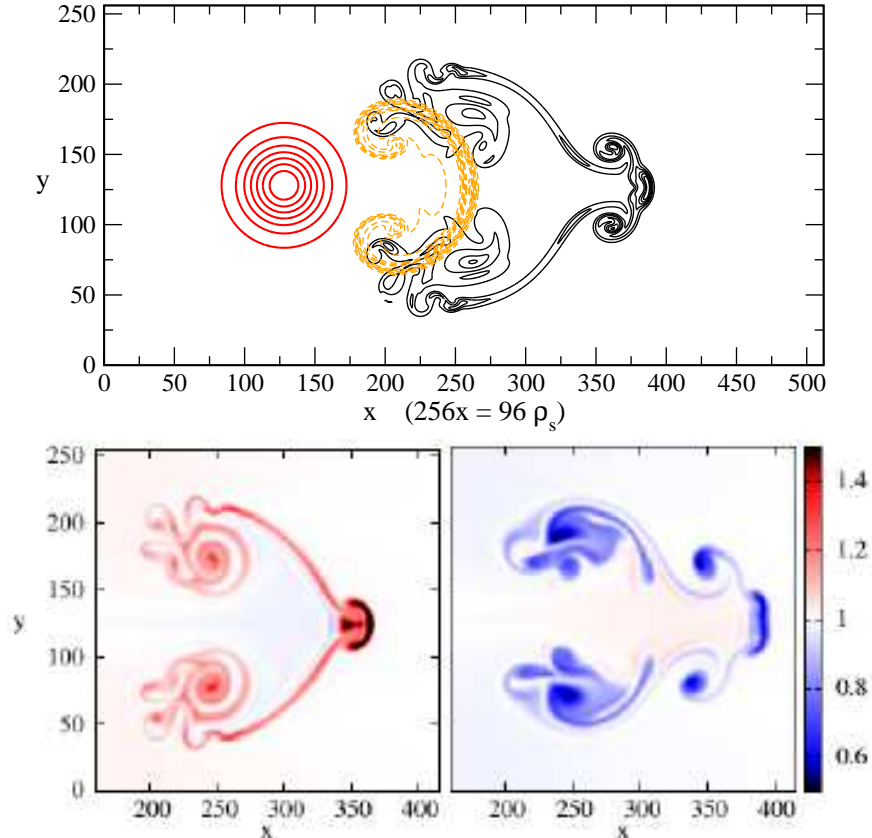


FIG. 1: Top (δn): Large amplitude blob/hole evolution in the δn model at $t=0$ (red bold), $t=12.5$ (orange dashed) and $t=25$ (black thin line). The contours of δn blob and hole coincide for simultaneous reversal of amplitude and x -direction. Bottom (n): different states of inertial blob (left) and hole (right: x -direction mirrored) at $t=25$.

The radial center of mass position is determined by

$$x_{center} = \left| \frac{\sum_{i,j} x_i [n_e(x_i, y_j) - n_b(x_i)]}{\sum_{i,j} [n_e(x_i, y_j) - n_b(x_i)]} \right| \quad (9)$$

and the center of mass velocity by $v_{center} = \Delta x_{center} / \Delta t$. The blob front position is here simply determined as the furthest outward x position where the density deviates more than 10 % from the initial background profile.

The acceleration occurs mostly in the initial quasi-linear phase (compare center-of-mass velocity plots in right figure), while at later times the center-of-mass velocities drop and the front velocities saturate nearly equally for blobs and holes.

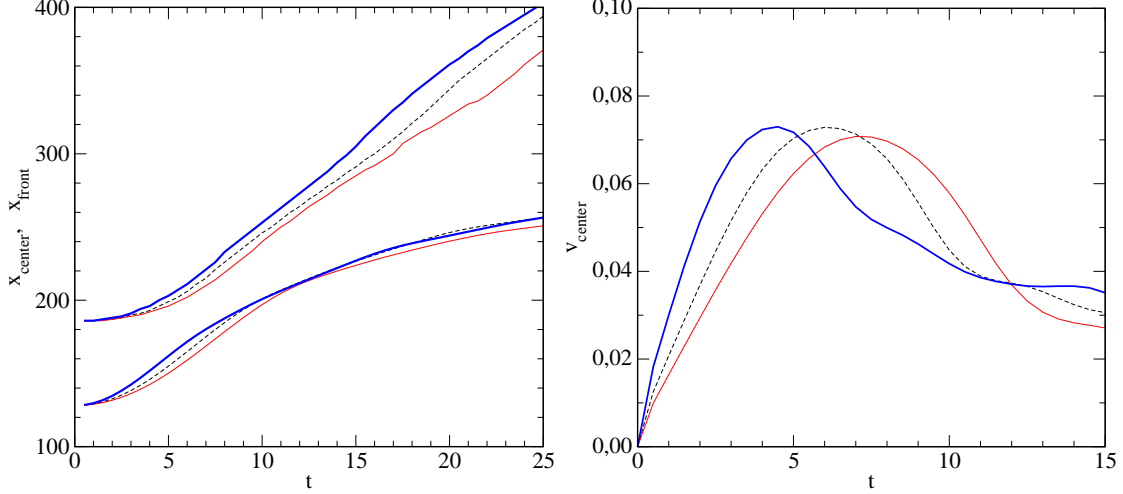


FIG. 2: *Left: time evolution of the center of mass (bottom lines) and propagation fronts (upper lines) for a delta-n blob (dashed black), inertial blob (thin red) and inertial hole (bold blue). Right: center of mass speeds. (Time in units L_{\perp}/c_s)*

The maximum center of mass velocity in general depends on the initial blob amplitude and width, which are here kept fixed. For given width and amplitude, the maximum velocities are found to be similar, with a slightly reduced maximum velocity for the inertial (full-n) blob compared to the delta-n blob, and a slightly increased velocity for the inertial hole. This observation is consistent with results for large amplitude blobs presented in ref. [14].

So far a constant background density has been assumed. Now a linearly decreasing background density profile $n_b(x) = 2(1 - x/x_{max})$ is considered. Blobs thus propagate into regions of lower background density, and holes into higher density. In a delta-n model the blob/hole velocity would be unchanged. Inertial blobs with

$$\frac{V_{full}}{c_s} \sim \sqrt{\frac{\Delta n}{(n_b(x) + \Delta n)}} \quad (10)$$

however can be expected to accelerate, and holes to be slowed down. For large enough gradients the inertial effects on blob/hole velocities found for flat profiles can even be reversed.

This is demonstrated in computations with $\Delta n = \pm 0.85$ and resolution $(128 \times 256)\rho_s$, with the initial blob/hole located in the middle of the domain, for otherwise identical parameters, in Fig. 3. The top figure shows a delta-n blob propagating down a density gradient at $t = 15$. In the bottom density contour plots (at $n = 1$) of the same delta-n blob (thin black line) and its anti-symmetric delta-n hole (dashed black line) are shown, together with a full-n inertial

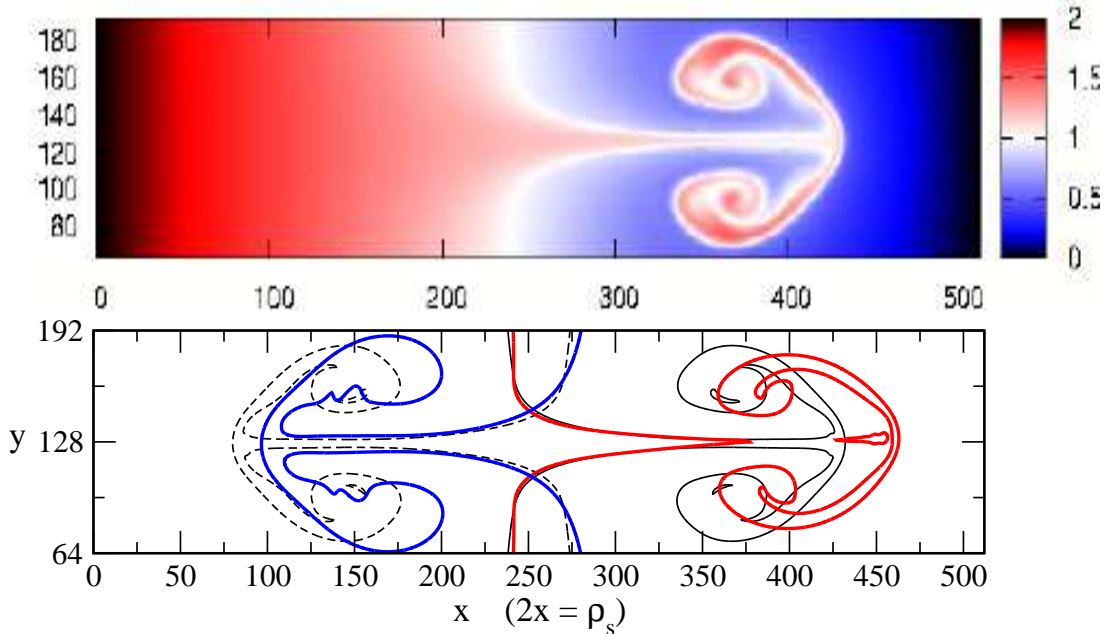


FIG. 3: *Top: delta-n blob evolved until $t = 15$ on a density gradient. Bottom: $n = 1$ density contour plots of the delta-n blob (thin black line), anti-symmetric delta-n hole (dashed black line), accelerated full-n inertial blob (bold red line) and decelerated full-n hole (bold blue line).*

blob (bold red line) that has accelerated further down the gradient (i.e. to the right side) and a full-n hole (bold blue line) which is slowed during propagation into denser regions.

To sum up these first results, in a delta-n model 2-d interchange blobs and holes evolve identically and regardless of a background density gradient. In the inertial full-n model, on a constant background the blobs move more slowly and coherently, and the holes faster and more fragmented.

On the other hand, on a background density gradient the inertial full-n holes, which move up the gradient, decelerate, whereas blobs accelerate down the gradient. The relative evolution and propagation of negative and positive perturbations thus strongly depends on the background gradient. Gradient steepening around the separatrix (where blobs and holes are most likely born) accordingly will lead to very different transport behaviour for full-n (or non-Boussinesq) models compared to results obtained in delta-n models.

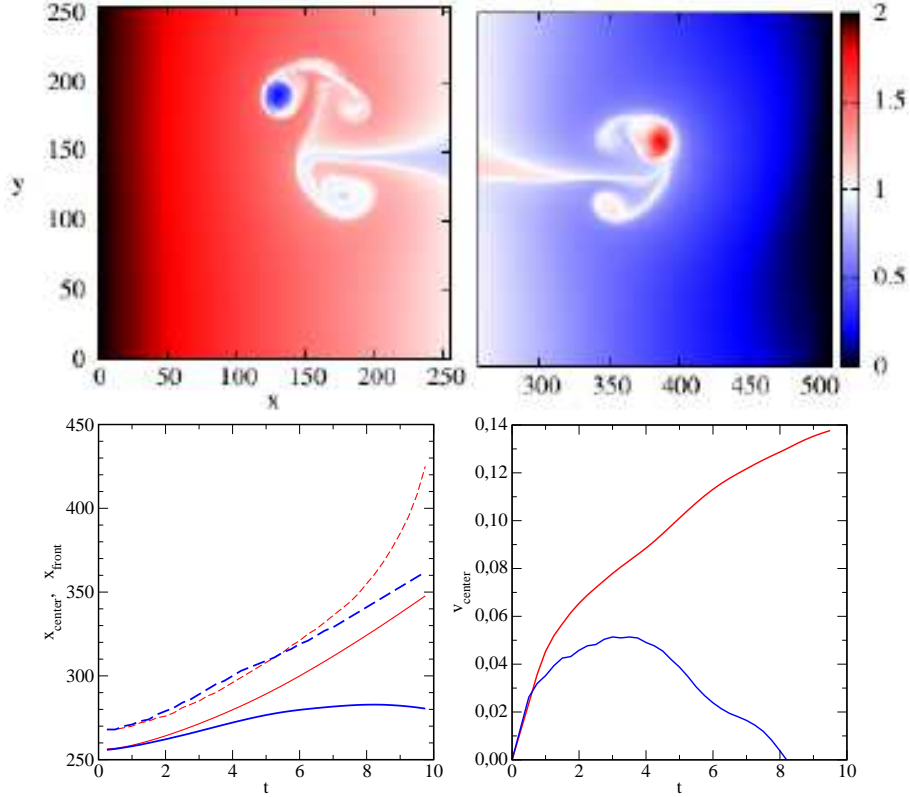


FIG. 4: *Top: Inertial large warm ion ($\tau_i = 2$) hole (left) and blob (right) on a density gradient: the more coherent head shows complicated poloidal-radial propagation. Bottom left: time evolution of the center of mass (bottom solid lines) and propagation fronts (upper dashed lines) for a inertial blob (red) and hole (blue, with x -direction inverted). Bottom right: corresponding center of mass velocities for the blob (red upper curve) and hole (blue lower curve).*

Next, the inertial evolution for warm ions with $\tau_i = 2$ is considered, which is a typical value for the tokamak SOL. Warm ions primarily enhance the blob propagation speed [18] by contributing to the interchange drive, break the (approximate) up-down symmetry through FLR effects on polarisation, and remain more coherent [14, 29]. Although the radial and poloidal propagation is more complicated (the hole head e.g. changes direction twice within the computation time), the major conclusions remain (Fig. 4): the inertial large blob center-of-mass velocity is larger than for the hole. The front velocity of the hole is initially higher than for the blob, but is reduced after sufficient propagation into the denser region.

IV. LARGE INERTIAL 3-D BLOBS, HOLES AND DRIFT VORTICES

3-d field-aligned computations of blobs and holes include different parallel electron and ion dynamics, which introduces charging and polarisation of the pressure perturbation, resulting in Boltzmann spinning of the blob [30].

The charging of a blob, which is initially localised in parallel direction, is a consequence of the higher parallel mobility of the electrons. In eq. (2) the acceleration $\partial_t v_s \sim 1/\mu_s$ is inversely proportional to the species mass, so that the resulting parallel current $J_{\parallel} \approx n_e e v_e$ is mostly carried by the electrons. In the absence of collisions ($C = 0$), electrons tend, according to the parallel component of eq. (2), towards a Boltzmann response with $\nabla_{\parallel} h = 0$, so that the electrostatic potential $\phi \sim \hat{n}_e$ spatially aligns with the blob. The resulting $E \times B$ drift leads to a perpendicular spinning vortex around the blob. For finite collisionality $C > 0$ the relative importance of spinning is controlled by the balance between the divergence of the parallel current and the divergence of the diamagnetic and polarisation currents under quasi-neutrality. The Boltzmann charging then is reduced, and depending on C the radial interchange drive competes with poloidal drift wave motion.

The present computations show that the spin-up of blob rotation by 3-d drift wave dynamics is strongly dependent on the collisionality parameter: for typical edge pedestal values in the closed-flux-surface region of $\hat{C} = 3.5$ the Boltzmann charging is dominant (cf. [16, 30]), but for an order of magnitude larger values ($\hat{C} \sim 20 - 50$), as more appropriate for mid-SOL plasmas, the interchange drive and the typical 2-d like blob plume structure actually prevail. In the presence of a density gradient, drift wave type propagation in the electron diamagnetic direction and instability add to the dynamics.

First, the flat background profile case with $\tau_i = 0$ (as in Fig. 1) is re-considered by extending the otherwise same computation to $n_z = 16$ planes in the field-aligned direction, including consistent poloidal (parallel) variation of the background magnetic field gradient $\kappa(z)$. The initial background density here is set constant in the parallel direction, and the initial electrostatic potential and parallel velocities are zero. The blobs are initially localised in the middle z plane.

For $\hat{C} = 7.5$ the Boltzmann spinning effect indeed is well pronounced, as shown in Fig. 5: the radial propagation is reduced compared with the 2-d (or a more strongly resistive) case. Holes charge up negatively and blobs positively, and obtain opposite Boltzmann spins. As

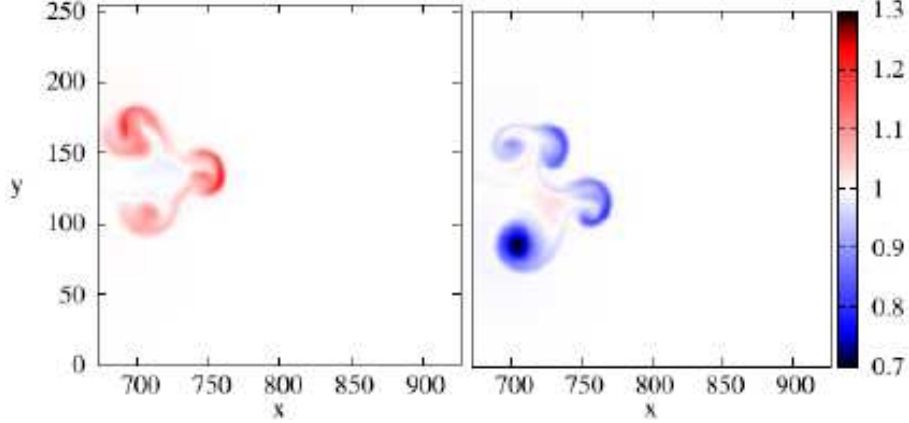


FIG. 5: 3-d computations at $t = 25$ of inertial blob (left) and hole (right, x-axis inverted) for $\hat{C} = 7.5$ and $\tau_i = 0$ (and otherwise same parameters as for Fig. 1) show strong Boltzmann spinning (which is significantly reduced for higher collisionalities).

the head is accordingly rotationally advected, the upper arm of the blob and the lower arm of the hole get more pronounced, respectively. It is also observed that the spinning hole shows stronger coherence than the blob.

Finally, the 3-d evolution of large amplitude ($\Delta n = \pm 0.85$) drift wave blobs and holes in a sheared slab geometry with $\hat{s} = 1$, $\kappa = 0$, $\hat{C} = 3.5$ and $\hat{\epsilon} = 18000$ on a background edge density gradient $n_b(x) = 1.5 - x/x_{max}$ is studied. The simulation domain is $(n_x \times n_y \times n_z) = (96 \times 256 \times 16)\rho_s$. Drift wave blobs show a rapid transition into fully developed turbulence. Here only the initial stage is considered.

For small amplitudes (or in a delta-n model) the development of nonlinear drift vortices is exactly CP-symmetric for initial blobs compared to holes (up to computing precision): the spatio-temporal contours are identical for reversal of the density gradient direction (P), while density fluctuation, potential and vorticity amplitudes are also reversed (C).

Fig. 6 on top shows the vorticity $\Omega = \nabla_{\perp}^2 \phi$ of blob (left) and hole (right) delta-n drift vortices at $t = 50$. Large drift wave blobs and holes however show different evolution in the consistent full-n model: the primary blob vortex (Fig. 6 bottom left) has spread and its amplitude is decreased compared to the delta-n case, whereas the hole vortex (bottom right) is compressed radially with a strongly increased vorticity amplitude. The hole actually can be observed as a coherent tripolar vortex for quite some time (multiple eddy turnover times) during the development into a fully turbulent state of the secondary drift wave structures.

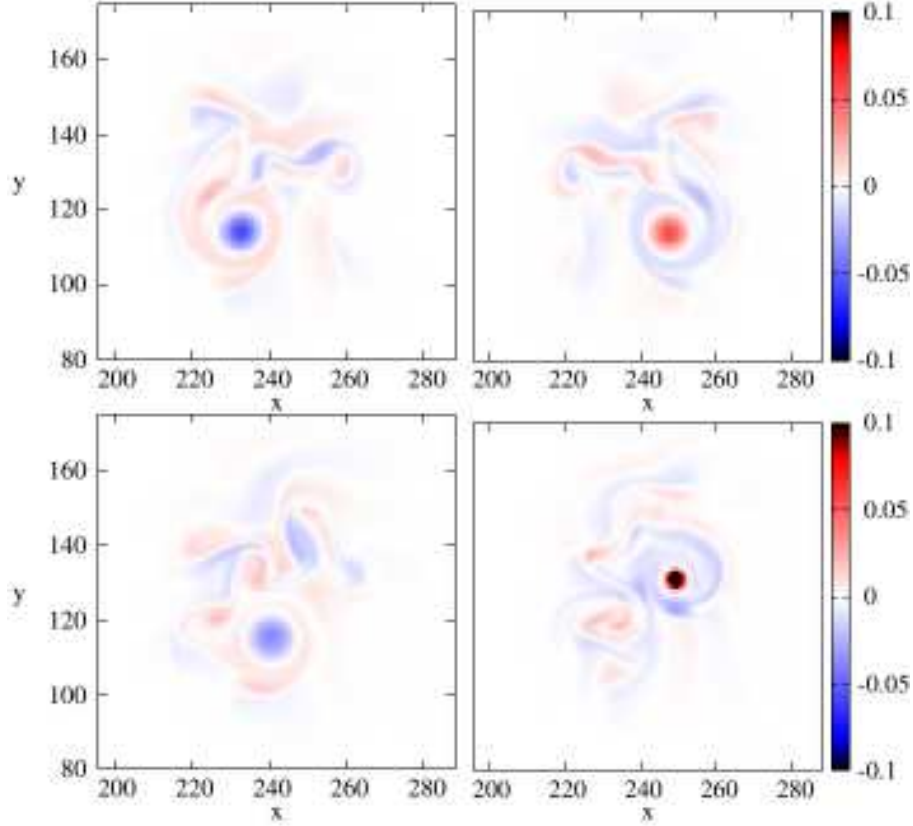


FIG. 6: Vorticity Ω of 3-d drift vortices evolved at $t = 50$ from large positive and negative density perturbations: in the delta-n model (top row) the blob (left) and hole (right) drift vortices are perfectly anti-symmetric. In the full-n model (bottom row) the negative initial vorticity of the blob has spread and its amplitude decreased. The positive vorticity of the initial hole is spatially compressed at increased amplitude. (Only part of the (x, y) domain at $z = 8$ is shown.)

As drift wave turbulence in the outer closed-flux-surface edge pedestal region near the separatrix can acquire fluctuations amplitudes in the same order of magnitude as the background, these results also show the relevance of full-n models for edge turbulence (and probably for the understanding of edge transport barriers) in addition to the relevance for modelling of SOL blobs and interchange turbulence.

V. CONCLUSIONS

To summarise, symmetry breaking between the evolution of magnetised plasma filaments with large positive (blob) and negative (hole) amplitudes has been found. Interchange blobs on flat density background have higher inertia than holes and propagate more slowly. In the presence of a large enough density gradient, blobs accelerate down the gradient and holes are slowed in their propagation up the gradient. Gradient steepening at the blob/hole birth region (supposedly near the separatrix) can thus lead to enhanced blob velocities and transport into the outer SOL. This mechanism would be consistent with observations at various tokamaks on an effect of core density increase on flattening of the outer SOL profiles [31, 32]. Another implication is that in the presence of a strong background gradient the inward impurity convection across the separatrix by holes can be reduced, and alignment of (trace and non-trace) impurities in vortices [33] can be expected to be significantly modified.

Full-n effects on large amplitude edge turbulence vortices, as they were demonstrated in this work, can lead to profound consequences. For example, large inward propagating holes can remain coherent on a turbulent background for significant times. It would be possible for such holes to be trapped on resonant surfaces (where they would not be filled up rapidly by parallel connection) and rotate for longer times with the background plasma. This could explain phenomena like palm tree modes [34].

Most of all, strong effects on the generation and structure of zonal flows (and, supposedly, mean flows) can be expected. As ion temperature fluctuations in the SOL also can achieve large amplitudes [35], both SOL and edge turbulence have to be studied with more complete source-driven full-n gyrofluid models including temperature and heat transport equations (or full-f gyrokinetic equations [36]), and with consistent coupling to the SOL including appropriate sheath boundary conditions. Such models are presently under development. The presented results clearly show the necessity for full-n, non-Boussinesq turbulence and blob transport models for the tokamak edge/SOL region.

Acknowledgements

The author thanks J. Madsen (DTU), M. Held and M. Wiesenberger (U Innsbruck) for useful discussions on full-n gyrofluid models. This work was partly supported by the Austrian Science Fund (FWF) Y398. This work has been carried out within the framework of the EUROfusion Consortium and has received funding from the Euratom research and training programme 2014-2018 under grant agreement No 633053. The views and opinions expressed herein do not necessarily reflect those of the European Commission.

-
- [1] P.H. Diamond, T.S. Hahm. *Phys. Plasmas* **2**, 3640 (1995).
 - [2] S.I. Krasheninnikov. *Physics Letters A* **283**, 368370 (2001).
 - [3] D. A. D'Ippolito, J. R. Myra, and S. J. Zweben. *Phys. Plasmas* **18**, 060501 (2011).
 - [4] P. Manz, T.T. Ribeiro, B.D. Scott, et al. *Phys. Plasmas* **22**, 022308 (2015).
 - [5] Y. Sarazin, Ph. Ghendrih. *Phys. Plasmas* **5**, 4214 (1998).
 - [6] J.A. Boedo, D.L. Rudakov, R.A. Moyer, et al. *Phys. Plasmas* **10**, 1670 (2003).
 - [7] B. Nold, G.D. Conway, T. Happel, et al. *Plasma Phys. Control. Fusion* **52**, 065005 (2010).
 - [8] O. E. Garcia, V. Naulin, A. H. Nielsen, and J. Juul Rasmussen. *Phys. Rev. Lett.* **92** 165003 (2004).
 - [9] O. E. Garcia, N. H. Bian, V. Naulin, et al. *Physica Scripta* **T122**, 104 (2006).
 - [10] M. Endler, H. Niedermeyer, L. Giannone, et al., *Nucl. Fusion* **35**, 1307, (1995).
 - [11] S. J. Zweben, D. P. Stotler, J. L. Terry, et al., *Phys. Plasmas* **9**, 1981 (2002).
 - [12] O. E. Garcia, J. Horacek, R. A. Pitts, et al, *Nuclear Fusion* **47**, 667 (2007).
 - [13] A. Kendl, B.D. Scott, and T.T. Ribeiro, *Phys. Plasmas* **17**, 072302 (2010).
 - [14] M. Wiesenberger, J. Madsen, and A. Kendl. *Phys. Plasmas* **21**, 092301 (2014).
 - [15] G. Q. Yu, S. I. Krasheninnikov, and P. N. Guzdar. *Physics of Plasmas* **13**, 042508 (2006).
 - [16] J. R. Angus and M. V. Umansky. *Phys. Plasmas* **21**, 012514 (2014).
 - [17] R. Kube and O. E. Garcia, *Physics of Plasmas* **18** 102314 (2011); and: **19**, 042305 (2012).
 - [18] P. Manz, D. Carralero, G. Birkenmeier, et al, *Physics of Plasmas* **20**, 102307 (2013).
 - [19] J. Madsen, *Phys. Plasmas* **20**, 072301 (2013).
 - [20] B.D. Scott, *Plasma Phys. Contr. Fusion* **45** A385 (2003).

- [21] A. Arakawa, J. Comput. Phys. **1**, 119 (1966).
- [22] G.E. Karniadakis, M. Israeli, S.A. Orszag, J. Comput. Phys. **97**, 414 (1991).
- [23] V. Naulin, A. Nielsen, SIAM J. Sci Comput. **25**, 104 (2003).
- [24] R.J. LeVeque, *Finite difference methods for ordinary and partial differential equations*. SIAM, Philadelphia, 2007.
- [25] J.R. Nagel, IEEE Antennas and Propagation Magazine **56**, 209 (2014).
- [26] S. Humphries, *Field solution on computers*. CRC Press, 1997. Electronic version: <http://www.fieldp.com/femethods.html> (last accessed: 10.02.2015).
- [27] B.D. Scott, Phys. Plasmas **12** 102307 (2005).
- [28] A. Kendl, Int. J. Mass Spectrometry **365/366**, 106 (2014).
- [29] J. Madsen, O.E. Garcia, J.S. Larsen, et al., Phys. Plasmas **18**, 112504 (2011).
- [30] J.R. Angus, M.V. Umansky, and S.I. Krasheninnikov, Contrib. Plasma Phys. **52**, 348 (2012).
- [31] B. Labombard, R. L. Boivin, M. Greenwald, et al, Phys. Plasmas **8**, 2107 (2001).
- [32] D. Carralero et al, Nucl. Fusion **54** 123005 (2014).
- [33] A. Kendl, Phys. Plasmas **19**, 112301 (2012).
- [34] H.R. Koslowski, B. Alper, D. N. Borba, et al Nucl. Fusion **45**, 201 (2005).
- [35] M. Kocan, F.P. Gennrich, A. Kendl, H.W. Müller and the ASDEX Upgrade Team, Plasma Phys. Contr. Fusion **54** 085009 (2012).
- [36] B.D. Scott, A. Kendl, and T.T. Ribeiro, Contrib. Plasma Phys. **50**, 228 (2010).